Journal of the Optical Society of America B
OPTICAL PHYSICS

Graphene-incorporated plasmo-thermomechanical infrared radiation detection

Mohammad Wahiduzzaman Khan, Qiancheng Zhao, Parinaz Sadri-Moshkenani, Md Shafiqul Islam, and Ozdal Boyraz*

Department of Electrical Engineering and Computer Science, University of California, Irvine, California 92697, USA
**Corresponding author: oboyraz@uci.edu*

Received 2 October 2019; revised 22 January 2020; accepted 27 January 2020; posted 28 January 2020 (Doc. ID 379154); published 19 February 2020

Metallic nanostructures can be used to selectively absorb a specific regime of the infrared (IR) spectrum depending on its constituent materials and geometry. In this paper, we propose and analyze a plasmo-thermomechanical detector that includes a graphene layer on top of metallic nanowires to enhance the absorption and sensitivity. The proposed device converts the free-space IR radiation to mechanical deformation of nanowires that modulates the insertion loss of the waveguide underneath the nanowires and facilitates the on-chip optical readout of the free-space radiation at room temperature. Our design takes advantage of localized surface plasmon resonances to maximize absorption at the desired IR spectrum. We provide a systematic investigation of different material combinations with and without graphene in addition to variations in detector geometry to optimize the designed IR detector. On top of the absorption enhancement, the graphene layer over the nanowires boosts thermal relaxation speed of the nanowires by 3 times due to graphene's high thermal conductivity, in turn speeding up the response of the IR detection. Moreover, the coated graphene layer enhances the mechanical deformation by a factor of 6 and bends the suspended nanowires downward, enhancing the light–matter interaction between the nanowires and the waveguide evanescent field. Overall, incorporating graphene is beneficial for enhanced spectrum absorption, speed of the IR detection, and optical readout sensitivity.

https://doi.org/10.1364/JOSAB.379154

1. INTRODUCTION

Over the past few decades, infrared (IR) detection [1] has been adopted for a wide range of applications [2] like night vision, missile tracking, noncontact thermal measurement, material inspection, defect detection, medical diagnostics, and so on. To meet the ever-challenging requirements set forth by these demanding novel applications, research has been carried out with a view to improving the application-specific [2] detection capability, sensitivity, selectivity, and efficiency. The advancement in single and compound semiconductor-based IR detectors has been largely favored by the precise fabrication methods and growth techniques developed by the integrated circuit (IC) industries. Recently, attention has been given toward novel materials [3–8] and nanoengineered structures [9–17] for enhanced IR sensing. IR detectors can be of two major types—photon detectors and thermal [18] detectors. The contemporary IR detectors are often bulky [1], cost-inefficient, and difficult to integrate, and most importantly require low temperature. IR detection based on temperature-induced [19,20] changes is, however, compact and cost-effective, and requires no cryogenic cooling, hence allowing highly desired room-temperature operation.

The photothermal way of IR detection relies on the conversion of electromagnetic energy into temperature or thermal gradient. This thermal effect can be gauged by the temperature-dependent physics such as changes in conductivity [21–23] or mechanical deflection [24,25]. Nanoengineered structures play an important role in the coupling between the different forms of energy as well as in determining the fundamental physics behind the transduction mechanism. For instance, in nanoscale, the increased surface to volume ratio of the nanostructures leads to a higher sensitivity as well as enhanced surface plasmons in plasmonic structures. Moreover, the dominant force acting on the system also changes at nanoscale allowing the occurrence of some interesting and utilitarian phenomena [26–28] such as quantum behavior, coulombic bending, highly reactive catalysis, and self-assembly of particles that are staggeringly different from macroscopic events. Geometric anisotropy [29–31] in nanostructures also manipulates the coupling and interaction between optical, mechanical, and thermal energy.

Specifically, at the nanoscale, we can take the advantage of mechanical deformation of structures in response to thermal gradient caused by free-space radiation absorbed by the structure. The challenge is to design a good absorber that can

efficiently and selectively absorb a specific regime of the radiation spectrum. This is where the plasmonic absorber [32–37] comes into play. For instance, A near-perfect optical absorption can be achieved even with ultra-thin plasmonic nanostructures [15]. Moreover, tuning the geometry and spatial distribution of such structures can lead to spectrally selective absorption [35], which is particularly beneficial for applications focusing on a narrow spectral region. In our design, we nanoengineer spectrally selective optical antennas in suspended metallic beams to absorb the free-space radiation. The antennas on a beam form a fishbone-like shape and convert electromagnetic energy to thermal energy, which creates a thermal gradient along the beam. The resultant thermal gradient, in turn, causes the beams to deflect based on its constituting material properties. We use a waveguide underneath, but not touching the suspended beams to optically probe the mechanical deflection that is proportional to the amount of the absorbed radiation, by means of evanescent mode coupling between the waveguide and the beams. The preliminary experimental results of the on-chip readout of the mechanical deflection caused by free-space radiation have been demonstrated [38]. We have proposed coating metallic nanostructures with graphene [39] in our device and investigated subsequent improvement in absorption and speed of operation due to graphene's extraordinary and potent thermal [40,41], optical [42], and mechanical [43,44] properties. Here, we present a comprehensive analysis of sensitivity, noise, and bandwidth improvement by incorporating graphene with metallic nanostructures. The variation of absorptance profile with respect to the variation in the size and shape of nanostructures is also discussed in detail. We show and include the effect of the adhesion layer in our calculation. In addition, the evanescent interaction and its effect on the waveguided probe signal are presented. We also compare numerically and analytically calculated time constants of the beam's mechanical deflection. The results indicate that, by integrating graphene in the nanostructure, the IR detector device can benefit remarkably in terms of sensitivity and speed of operation.

2. DEVICE MODEL

The proposed optomechanical device consists of a 1.5 μm wide and 0.3 μm thick Si_3N_4 waveguide and an array of graphene-coated suspended metallic fishbone nanowires above, as illustrated in Fig. 1. The experimental demonstration [38] consisted of bimetallic antennas without a graphene layer having 20 nm nickel and 30 nm gold for optimized maximum deflection in response to radiation. As the free-space radiation is applied on the nanowires, the plasmonic resonant absorption by the integrated antennas creates a thermal gradient along the nanowires. The temperature reaches maximum at the middle of each of the nanowires; this is also the maximum deflection point as expected. The mechanical deflection causes the gap between the waveguide and suspended metallic structures to vary. The coupling between the evanescent waveguide mode to the nanowires changes depending on the gap that in turn changes the insertion loss of the waveguide. Thus, the free-space IR radiation can be measured by sensing the probe light through the waveguide. The whole system can operate at room temperature and can be integrated on the silicon platform.

The sensitivity of the device is measured by the absorption efficiency of free-space radiation. For an absorption coefficient of 0.338 of the designed antenna [38] at near IR, the bimetallic nanowires were estimated to deflect ~ 15 nm. The sensitivity of the insertion loss of waveguide (S_{21}) was experimentally measured to be 4.3×10^{-3} nm^{-1} in the same work. To increase the sensitivity, we propose to incorporate graphene to the nanowires. Graphene is a 2D material that is simultaneously flexible and strong, and carries extraordinary optical, thermal, and mechanical behavior. Our IR detector employs optically induced thermomechanical fluctuations to measure the radiation. Therefore, graphene's properties can be exploited and utilized here. The interplay between graphene and metallic nanostructures has already been proven to be beneficial. Single-layer graphene absorbs radiation weakly because of its short interaction length. Even so, the enhanced performance of graphene-based photodetectors [45,46] has been achieved by introducing metallic nanostructures on the detectors to selectively enhance the absorption of radiation and thus the photocurrent. Similarly, metallic absorbers have seen an increased absorption coefficient when graphene is incorporated in the system [47] facilitating high-sensitivity plasmonic detection and biosensing. Furthermore, the enhanced interaction between graphene and waveguided light [48] has spurred significant interest in graphene-based on-chip optical communication devices. We investigate different metallic nanowire and graphene combinations. We have shown over twofold absorption enhancement by considering a single-layer graphene sheet over the nanowires. This large enhancement is not simply the result of adding a single-layer graphene sheet as it absorbs only 2.3% of the radiation over a broad wavelength range. We see higher enhancement for thinner metallic films. The reason is that thinner nanowires allow more interaction between the graphene layer on top and the generated localized surface plasmons.

The temperature created by the absorbed radiation dissipates mostly by conduction. Heat is conducted from the nanowire midpoint to the pads. The temperature at this point has been calculated to rise up over 400 K in some cases. Because of the large area of the pads supporting the suspended nanowires, they are considered to be at ambient temperature (293.15 K) for modeling purposes. The heat dissipation is important since the speed of the device operation depends on the thermomechanical relaxation of the nanowires. Having the graphene layer on top of the nanowires again proves to be beneficial in this regard, as graphene has a very large thermal conductivity (> 5000 $Wm^{-1}K^{-1}$ reported [40]) that leads to faster heat spreading and accelerated thermal response of nanowires.

Strip antennas are designed and optimized for resonant radiation absorption by varying the antenna dimensions. The unit cell is shown in the Fig. 1 inset along with the field distribution at resonant plasmonic absorption. By default, we set the width of the beam and antenna equal, $W = Wb = Wa = 100$ nm, antenna length, $L = 350$ nm, and period $P = Px = Py = 660$ nm. We see the resonance shift by changing the period and length of the antenna. As discussed in a later section, the longer antenna length and (or) the larger antenna period result in longer resonant wavelength. Multiple strip antennas are placed along the nanowires to augment the

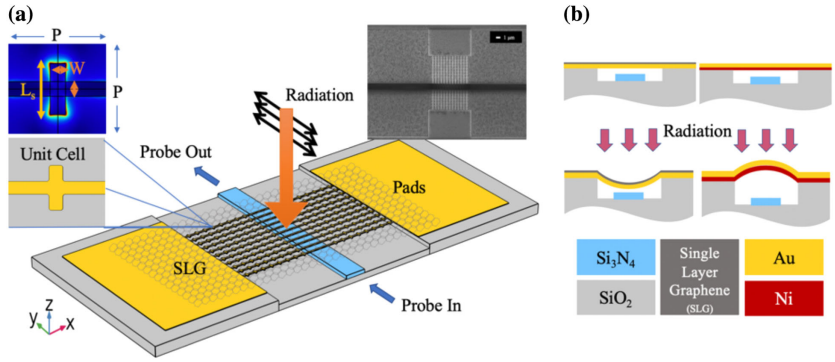

Fig. 1. (a) Geometry of the whole system: the fishbone nanowire array with graphene is suspended above a Si_3N_4 waveguide. The plasmonic nanowires selectively absorb free-space IR radiation. The inset shows the unit cell (graphene layer not shown) and its field distribution at resonant absorption. Inset on the right shows the SEM top view image of the detector containing fishbone suspended metallic nanostructures and the waveguide. (b) Plasmonic heating causes the suspended layer to expand and mechanically deflect, modulating the gap between waveguide and plasmonic structures. The insertion loss of the waveguide thus reflects the incident radiation. The deflection magnitude and direction depend on the thermal expansion coefficients of the materials.

total absorption. The number of strip antennas in a beam is chosen so as to keep a balance between temperature buildup and deflection. The number of nanowires is also optimized to give an optimized amount of waveguide insertion loss. The fabricated device consisted of 11 of the 12.54 μm long nanowires each holding 16 strip antennas to produce enough mechanical deflection and modulation of the S_{21} parameter.

3. FABRICATION AND EXPERIMENTAL CHARACTERIZATION

The proposed approach of free-space radiation detection has been verified by an experimental demonstration [38] that includes bimetallic suspended nanowire fishbone as antennas and Si_3N_4 waveguides as a readout circuit. At the beginning of fabrication, oxide, nitride, and cladding oxide layers are grown or deposited by thermal oxidation, low-pressure chemical vapor deposition (LPCVD), and plasma-enhanced chemical vapor deposition (PECVD), respectively. Photolithography and dry etching are done to pattern the waveguide. The bump on the PECVD oxide due to the waveguide is removed by chemical–mechanical polishing (CMP) and dry etching. Then e-beam lithography is done to pattern a fishbone structure on PMMA resist. After that, metal evaporation and liftoff, hydrofluoric (HF) vapor etching was done to etch the sacrificial SiO_2 layer between the nanowires and the waveguide top facet, thus creating a suspension of nanowires.

The fabricated IR detector is characterized experimentally [38] by measuring the power output of the waveguide. A continuous wave (CW) of 1550 nm (probe) passes through the waveguide with its evanescent fields modulated by the mechanical vibration of the nanowires upon the incident radiation from the laser diode (LD) of 660 nm. We tune the LD modulation frequency and record the voltage from the lock-in amplifier connected to the power meter at waveguide output end. We calculate the 3 dB bandwidth of the detection scheme as 9.6 Hz and a time constant of $\tau = \frac{1}{2\pi f_{3\,\mathrm{dB}}} = 16.6$ ms. The results are shown in Fig. 2. The voltage reading with respect to LD frequency appears in Fig. 2(a). We show the sinusoid-like time trace of the filtered power in Fig. 2(b) as the incident radiation is also a sinusoid.

We also report the normalized correlation between the input sinusoid to the waveguide output signal in Fig. 2(c). At higher incident power intensity, the correlation is better, and the modulation index is also higher. In the inset of Fig. 2(c), we can see how well correlated the waveguide output power and LD modulation signal is. Correlation is a metric of how well the detector sensed the time-varying radiation. To illustrate the modulation strength for different levels of radiation power—21.15, 55.05, and 87.91 mW—we show the FFT. The relative power of the sideband is a measure of the modulation index or modulation strength. We can see the sideband at the modulation frequency (0.05 Hz) is prominent for higher radiation intensity, and it eventually drops below the system-induced noise floor at a radiation power lower than about 20 mW.

4. ABSORPTION ENHANCEMENT BY GRAPHENE

Graphene-based photodetectors are limited in terms of absorption due to infinitesimal overlap between photon waves and this monolayer 2D material. However, graphene's absorption can be further enhanced [13,14] if it is coupled with the proposed antennas. Here, we use the finite-element method (FEM) to calculate the absorption coefficient of different metallic nanostructures with and without the graphene layer on them. In particular, we use the fishbone or cross geometry because they are easier to fabricate and suspend, and they also show strong plasmonic absorption. We numerically calculate the absorptance using a single unit cell with proper periodic boundary conditions along the repetitive directions and perfectly matched layer (PML) boundary condition along the direction of propagation. Being a cross-shaped structure, the absorber unit cell contains sharp corners that may lead to electromagnetic singularity. To avoid singular electromagnetic field results, and to resemble a realistic fabricated sample, we have included rounded edges at the corners as shown in the unit cell inset of Fig. 1(a). This allows more precise and realistic predictions of the device characteristics. For the numerical analysis, graphene

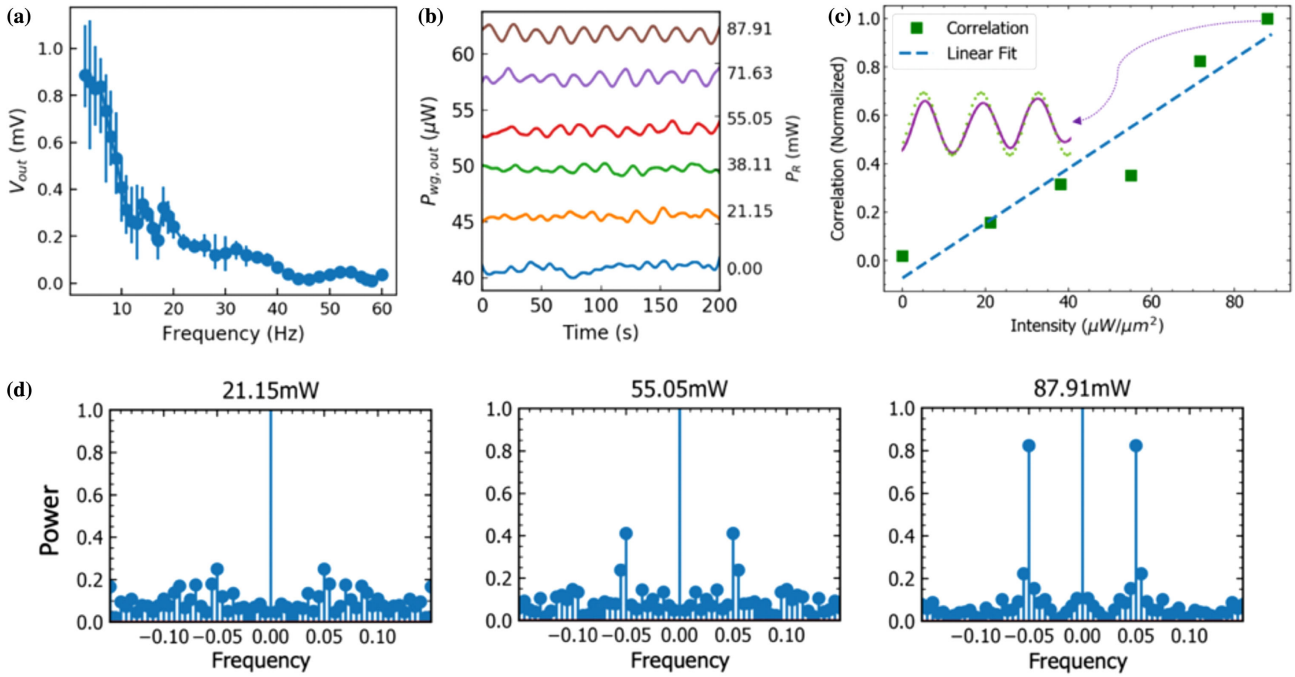

Fig. 2. (a) Frequency response of the output voltage obtained from a lock-in amplifier that indicates the waveguide output power. (b) The digitally filtered waveguide output power $P_{wg,\text{out}}$ for different levels of radiation power, P_R. The $P_{wg,\text{out}}$ at different radiation levels have similar average power but are offset along the y axis according to the radiation power for clarity. The right y axis indicates the incident radiation power. Radiation power is considered to be 0 in the nonillumination case. (c) The correlation between the filtered detected power variation with respect to sinusoidal incident radiation as a function of the peak intensity. Inset shows the incident sinusoidal radiation (dotted green) and detected filtered waveguide output (solid violet), which is the case for a radiation power of 87.91 mW. (d) FFT of raw detected signal for different levels of incident radiation showing sidebands at 0.05 Hz (the modulation frequency), x axis is frequency in Hz, and y axis is power in arbitrary unit. Higher incident radiation gives higher sidebands, thus higher modulation index.

is considered as a 2D conductive sheet where the conductivity of graphene is modeled as [49]

$$\sigma(\omega) = \sigma^{\text{intra}}(\omega) + \sigma^{\text{inter}}(\omega)$$
$$= i\frac{2e^2 k_B T}{\pi\hbar\omega}\ln\left[2\cosh\left(\frac{\mu_c}{2k_B T}\right)\right]$$
$$+ \frac{e^2}{4\hbar}\left[u(\hbar\omega - 2\mu_c) - \frac{i}{2\pi}\ln\frac{(\hbar\omega + 2\mu_c)^2}{(\hbar\omega - 2\mu_c)^2) + (2k_B T)^2}\right], \quad (1)$$

where σ^{intra} is intraband conductivity and σ^{inter} is interband conductivity. Here, the step function u determines the interband electron transition, k_B is the Boltzmann constant, $\hbar$ is the reduced Planck's constant, e is the electron charge, and T is temperature, and we assume a chemical potential of graphene, $\mu_c = 0.45$ eV, a relaxation time of ~ 0.5 ps, a Fermi velocity of 9.5×10^5 ms^{-1}, and a mobility of 9000 $\text{cm}^2\,\text{V}^{-1}\,\text{s}^{-1}$.

As evident from Fig. 3, coating graphene on nanostructures significantly enhances the plasmonic absorption. We observe over 33% enhancement in absorptance when graphene is integrated on 20 nm thick silver fishbone nanowires. This increased absorption of radiation causes a larger temperature gradient, larger mechanical deflection, and, as a result, larger modulation of probe light at the waveguide output. For bimetallic nanowires, the ratio between the thicknesses of gold and nickel is kept 1.5 to obtain maximum deflection. However, the absorption does not change much for graphene–nickel or graphene–gold–nickel fishbones. This can be attributed to broader plasmonic absorption by nickel antennas [50]. However, single metal fishbones also give a comparable level of absorption with an even thinner material layer. This is even more beneficial as using a single metallic nanostructure reduces the fabrication steps and complexity in comparison to bimetallic ones while achieving a higher or the same level of absorption performance with the aid of graphene coating.

Since a titanium (Ti) layer of 3 nm is used as an adhesion layer during the bimetallic layer deposition for the actual fabrication of the designed IR detector, we consider the effect of this very thin layer in our numerical calculation of absorptance. This adhesion layer is indispensable for depositing metal films, particularly gold films, and almost all of the time, their effect is overlooked as the thickness is negligible compared to other material layers. As we are using an atomically thin graphene sheet in our proposed design, we also examine the effect of having Ti in our FEM study. In the inset of Fig. 3(d), we see that the adhesion layer Ti does not have any effect on the absorptance spectrum. The solid line represents the absorptance with Ti considered, and the circle markers represent the absorptance without the Ti layer.

The geometry of nanostructures can be adjusted to tune the absorption spectrum. We scrutinize the variation of the antenna length, width, and shape. We already have an idea of how the thickness variation for different materials influences

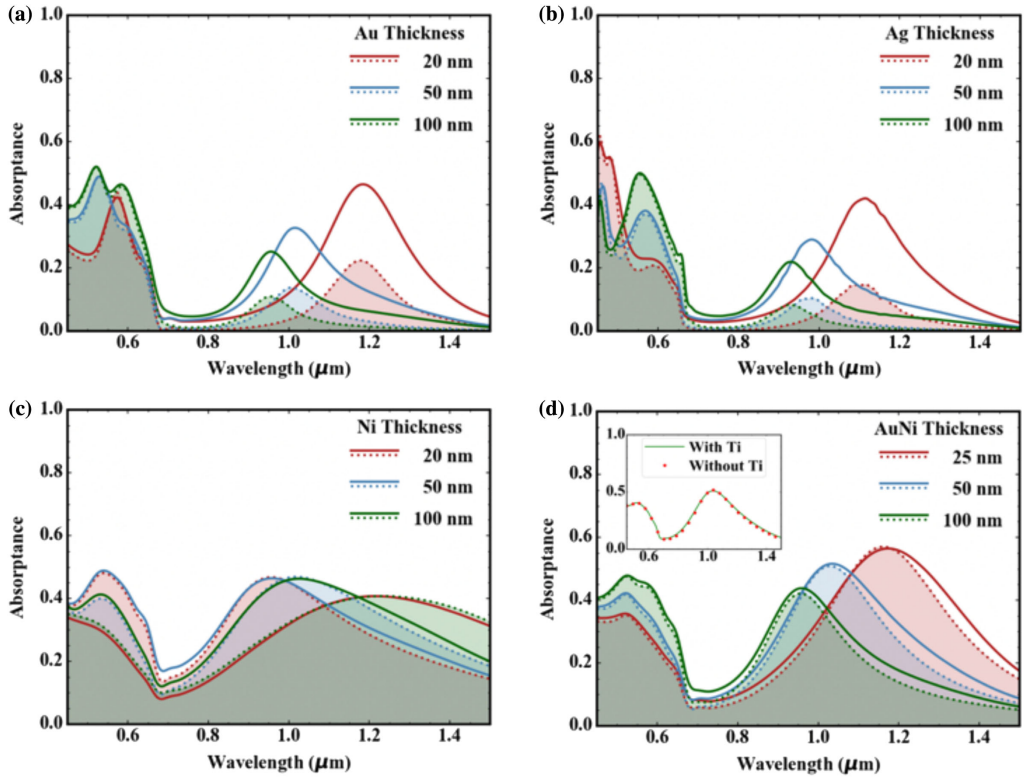

Fig. 3. Absorptance of suspended fishbone nanostructures with (solid) and without (dotted-filled) graphene coating for different metals—(a) gold, (b) silver, (c) nickel, and (d) gold–nickel of varied thickness. Inset of (d): the effect of adhesion layer titanium (Ti) on the numerically calculated absorptance of the bimetallic fishbone.

the response from Fig. 4. As the thickness is increased, the plasmonic coupling between the top and bottom surfaces of the nanowires decreases, so does the plasmonic absorption. The absorption peak also shows a blue shift. As the incident radiation has a polarization along the direction of the antenna, the antenna length can be tuned to tune the absorptance. The absorption peak expectedly shifts with the antenna length. This is shown in Fig. 4(a). The purpose of the beam is to hold the strip antennas. However, the size of the beam impacts the plasmonic oscillation or resonance, which is depicted in Fig. 4(b). The wider beam reduces the absorption peak and causes a blue shift of the absorption spectra. Finally, to peruse the high absorption coefficient at the lower wavelength (450–670 nm), we solve the absorptance for different shapes of the suspended metal films. From our observation of Figs. 4(c) and 4(d), we attribute that high absorption to the materials' inherited plasmonic property. However, the primary absorption peak around 1 μm is obviously because of the strip antennas as seen from Fig. 4.

5. SENSITIVITY ANALYSIS

We also study sensitivity of the proposed devices with different materials in combination with graphene coating. The sensitivity of the detector depends on the amount of evanescent coupling between the waveguide and nanostructure. We define a performance variable called the evanescent intensity ratio (EIR), Fig. 5(a), which is the ratio between the power of the leaked mode in the nanostructure to the total power. A higher EIR means more wave leaks and interacts with the metallic fishbone. The evanescent field and guided mode are shown in Fig. 5(b).

We also report the variation of transmittance, Fig. 5(c), through the waveguide as a function of distance (gap) between the waveguide top facet and a single-beam metallic fishbone. A higher EIR gives higher modulation of the transmission through the waveguide. So, it is beneficial to suspend the beams not too far above from the waveguide top facet.

The detector configured with a 50 nm gold fishbone coated with graphene deflects 120 nm for a beam centerpoint temperature change of 82 K giving us a deflection of 1.46 nm/K for an incident radiation of 68 $\mu W/\mu m^2$ intensity. This is almost an order more deflection than out of an earlier report [38]. The deflection for 1 $\mu W/\mu m^2$ is calculated to be $z_{vib} = 1.76$ nm/($\mu W/\mu m^2$). Fig. 5(c) further gives the idea of waveguide output modulation because of this vibration, and it clearly depends on the rest gap between the waveguide and the nanostructure. We calculate over a 0.1% change in waveguide output power for a change in radiation intensity of 1 $\mu W/\mu m^2$ with only a single beam of fishbone. Nickel- and gold–nickel-based nanowires show higher plasmonic interaction. We can also incorporate an array of the fishbone beams to get higher modulation strength at the waveguide output.

6. NOISE ANALYSIS

The plasmo-thermomechanical detector we designed is affected by three different noise sources—thermal, ambient, and

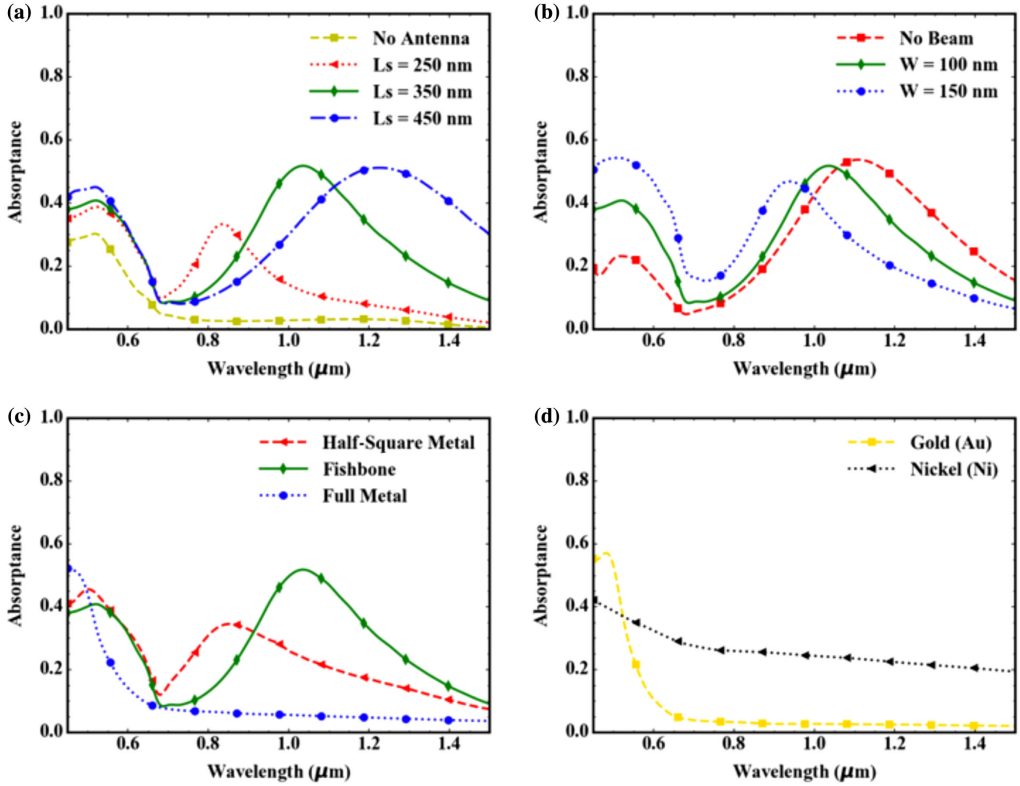

Fig. 4. Absorptance adjustment by geometric tuning of suspended fishbone nanostructures: (a) variation of strip antenna length, L_s, without the antenna there is no absorption peak near 1 μm; (b) variation of beam width, W; (c) suspended metal shape; and (d) absorption due to unpatterned suspended continuous gold and nickel film clarifying the high absorptance at lower wavelength in rest of the plots.

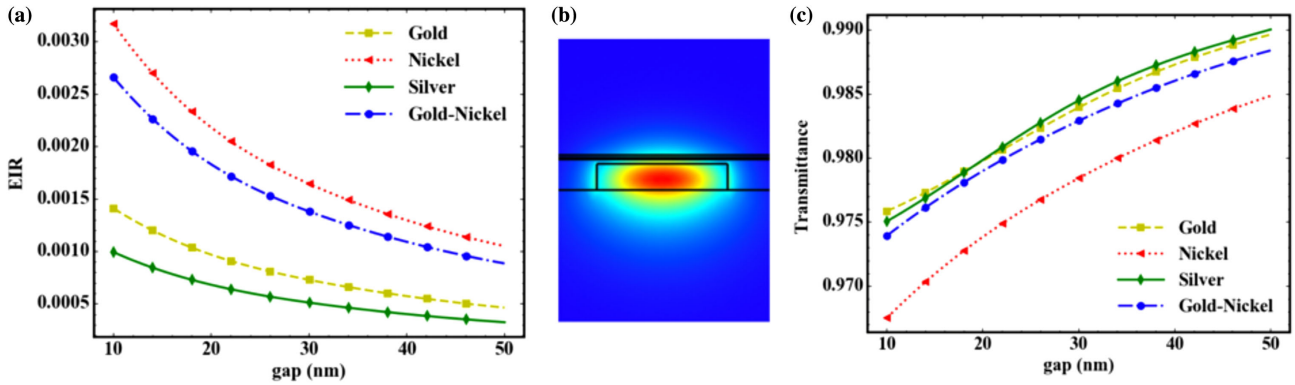

Fig. 5. Sensitivity analysis: (a) evanescent intensity ratio (EIR) for different material nanostructures as a function of gap; (b) field view showing guided mode and field leakage to the nanowire region above the waveguide; and (c) transmittance modulation as a function of the gap between waveguide and fishbone nanostructures for a single beam containing nanowires. Higher EIR causes larger change in the insertion loss of the waveguide.

mechanical. The thermal noise is dependent on the temperature and equivalent thermal conductivity of the device along the thermal path of interest. With graphene, we get a thermal noise power of $P_{\text{th}} = \sqrt{4k_B T^2 G} = 4.74\ \text{pW}/\sqrt{\text{Hz}}$, where we consider thermal conductance G through air, gap, and substrate, and primarily along the nanobeams, k_B is the Boltzmann constant, T is the temperature. The contribution of graphene's large thermal conductivity to this noise is compensated by its tiny cross-section. Ambient noise caused by radiative heat transfer to and from the device is negligible as the temperature build up is not too high. To analyze the mechanical noise, we calculate the equivalent Young's modulus of the nanowire to be $E = 137$ GPa. This results in $0.68\ \text{fm}/\sqrt{\text{Hz}}$ of nonresonant vibrational noise by using $z_{\text{noise}} = \sqrt{\frac{24k_B Tl^3}{\pi^4 w\omega_o t^3 E Q}}$, where l, w, and t are the length, width, and thickness of the nanowire, Q is the quality factor obtained from simulation of the nanowire, and ω_o is the resonant frequency. The power of vibrational noise thus appears to be $P_{\text{vib}} = \frac{z_{\text{noise}}}{z_{\text{vib}}} A$, where A is the $12.54 \times 8.58\ \mu\text{m}^2$ detector footprint. P_{vib} is calculated to be $41.57\ \text{pW}/\sqrt{\text{Hz}}$,

which is more than 7 times smaller than previously reported [38]. The overall device noise is thus dominated by the mechanical vibration of the device. However, the experimental result [38] and ambient condition suggest high system level noise coming from the air flow chamber that is used to keep the device free from dirt particles, optical table vibrations, and other microphonic sources. In the practical setting, the detector would be implemented in a vacuum-sealed environment eliminating or reducing the possibility of contribution from different external noise sources.

7. GRAPHENE'S EFFECT ON THERMAL RELAXATION TIME

Graphene has a very large thermal conductivity [40] of over 5000 Wm^{-1} K^{-1}. The suspended graphene especially shows almost 1 order higher [51] thermal conductivity than the supported graphene. The large thermal conductivity allows graphene to quickly conduct heat from one position to another. So, graphene can work as a heat spreader [52] that can enhance the extraction of heat out from the plasmonic hotspots. Thus, having a graphene layer on top of the fishbone nanowires proves to be even more useful since this quicker extraction of heat causes faster thermal relaxation. Absorbing the free-space radiation, the fishbone nanowires deform due to the temperature gradient created along it. The heat dissipation mechanism is mostly conductive. The mechanical relaxation of nanowires upon the removal of the incident free-space radiation depends on how fast the heat can be dissipated. So, graphene allows the faster device operation when there is any time-varying radiation. The time-dependent study for nanowires of 50 nm thickness (for gold–nickel bimetallic nanowire, we consider 30 nm gold above 20 nm nickel) is shown in Fig. 6. Comparing Fig. 6(b) to Fig. 6(a), we observe a faster thermal oscillation resulting from a substantial reduction in the rising and falling time constants when graphene is incorporated in the nanowires. For gold and silver nanowires, thermal buildup from the absorptance enhancement [Figs. 3(a) and 3(b)] by graphene dominates the thermal escape from the heat-spreading property of graphene. The opposite happens for nickel and gold–nickel nanowires as they do not see significant enhancement in absorptance [Fig. 3(c) and 3(d)]. In Figs. 6(c) and 6(d), we set the nanowire at an arbitrary but anticipated temperature gradient as an initial condition and then observe how the temperature profile along the beam varies with time. We clearly observe that for a given temperature gradient, the device coated with graphene cools down much faster than the one without, allowing faster operation of the detector.

To calculate the thermal time constant, we assume the convective and radiative heat transfer effects to be negligible in this system as their thermal resistances are more than 4 orders of magnitude higher than the thermal conduction resistance. For all nanowires considered in the analysis, the thermal time constants deduced separately from simulation and analytical

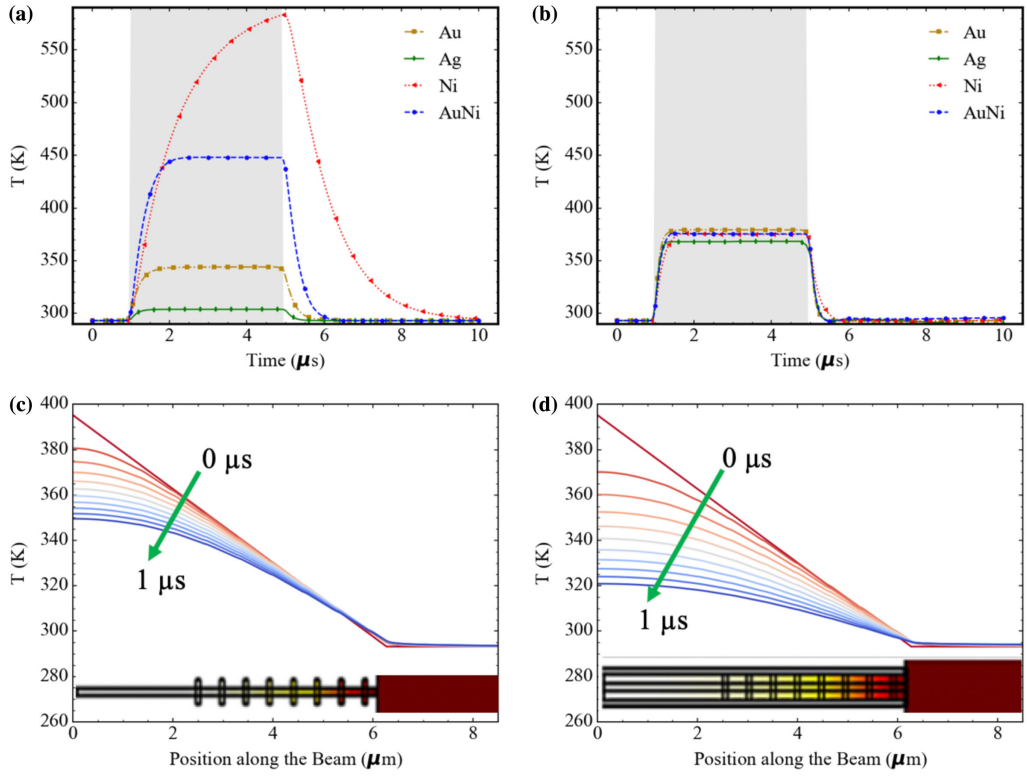

Fig. 6. Time-dependent study of the IR detector: (a-b) temperature at the midpoint of different nanowires (a) without and (b) with graphene coating based on a given radiative pulse of 4 μs width. The shaded region shows the pulse duration. (c-d) Spatial temperature profile along the gold–nickel beam (c) without and (d) with graphene for a given initial thermal distribution (0 μs). In both cases, the top view of the beam is placed as an inset, and the beam's geometric coordinates are aligned with the x axis. With graphene, the profile cools down to a much lower temperature for a given time of 1 μs [39].

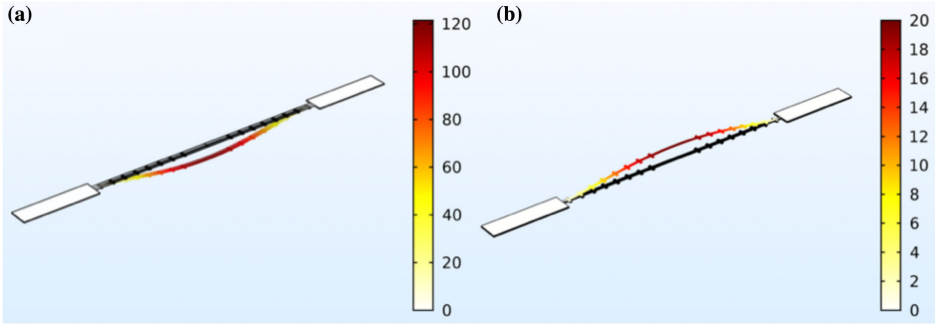

Fig. 7. Nanowire deformation (nm) (a) with and (b) without graphene.

calculation are observed to be in agreement. As an example, we report the thermal time constants of the gold–nickel nanowire with and without graphene calculated analytically and from simulation-obtained Figs. 6(a) and 6(b). Our finite-element simulations show that the temperature distribution of the gold–nickel fishbone structure varies with a thermal time constant of ~ 0.42 μs for rising edge and ~ 0.45 μs for falling edge. The total temporal width in this case is ~ 0.87 μs. If graphene is incorporated, the time constant becomes ~ 0.13 μs for rising edge and ~ 0.15 μs for falling edge, which is 3 times less than the case without graphene. In this case, the total temporal width is ~ 0.28 μs. Therefore, a coating graphene sheet can boost the device thermal response speed by 3 times. The conclusion from the numerical study aligns with our analytical results, in which a twofold speed enhancement is derived based on the thermal time constant calculation for multilayer thin films under periodic heating [53]. Based on thermal circuit analysis,

$$\tau = R \times C = \frac{L}{kA}\rho C_p V = \frac{L^2}{\alpha}, \tag{2}$$

$$\alpha = \frac{\sum k_i h_i}{\sum \rho_i C_i h_i}, \tag{3}$$

where R is the thermal resistance, C is the thermal capacitance, and α is the effective thermal diffusivity. Here, L is assigned to be 6.27 μm (half of the total length due to symmetry), i is material index (gold, nickel, graphene), ρ is material density, V is volume, h is thickness, and C_p and C_i are specific heat. Gold and nickel have a bulk thermal conductivity [54] of 318 $\mathrm{Wm^{-1}\,K^{-1}}$ and 90.7 $\mathrm{Wm^{-1}\,K^{-1}}$, respectively. To capture more realistic thermal conductivities [55], we consider all the scattering mechanisms (thickness, boundary, and grain size) that result in $k_{\mathrm{Au}} = 170$ $\mathrm{Wm^{-1}\,K^{-1}}$ and $k_{\mathrm{Ni}} = 60$ $\mathrm{Wm^{-1}\,K^{-1}}$. The calculated diffusivities are 4×10^{-5} $\mathrm{m^2 s^{-1}}$ and 7.3×10^{-5} $\mathrm{m^2 s^{-1}}$ without and with graphene, respectively, resulting in ~ 1 μs and ~ 0.5 μs of the time constant. The small difference between the numerical and analytical calculation can be attributed to that in analytical calculation the change in cross-section along the beam is not taken into account. For the time-dependent thermal analysis, the ambient temperature is considered to be 20° C or 293.15 K. The higher thermal conductivity of graphene limits the maximum temperature buildup. However, graphene-enhanced absorptance and the large contrast between the thermal expansion coefficients of graphene (-8×10^{-6} $\mathrm{K^{-1}}$) and the candidate metals ($13 - 18 \times 10^{-6}$ $\mathrm{K^{-1}}$) allow for a large deflection in the graphene-coated nanowire resulting in higher sensitivity of the detector.

8. MECHANICAL DEFLECTION INCREMENT

As graphene has a negative thermal expansion coefficient, coating graphene over metals will result in downward deflection of the nanowire beam when it absorbs radiation. So, suspension should be created far enough from the top facet of the waveguide in order to avoid collision. We also numerically calculate the maximum von Mises stress of 40–130 MPa, which is within the yield point of the materials in consideration. Therefore, we do not expect any significant plastic deformation of the nanowires. Figure 7(a) and 7(b) show the beam deformation for graphene on 50 nm thick gold (max. 120 nm downward) and 50 nm gold–nickel (max. 20 nm upward) nanowires, respectively, when the incident radiation of 68 $\mu W/\mu m^2$ intensity is at a wavelength that gives maximum absorptance. We see a sixfold beam deflection in the graphene-coated beam that translates to increased sensitivity of the IR radiation detection.

The higher defection causes larger modulation of the light through the waveguide. This results in higher sensitivity and modulation index of the detector, enhancing the detection sensitivity of the device.

9. CONCLUSION

The graphene-coated nanostructure is shown to be beneficial in manifold perspectives including the easy integration, enhanced sensitivity, and room temperature operation. For the IR detector we propose, we observe significant improvement in sensitivity in the form of absorptance increment, as well as in speed in the form of a low thermal resistance heat dissipation path. We numerically and analytically calculated and compared the absorptance for graphene-metal nanowires and their time constants of the thermal oscillation. In addition to its benefits, graphene is inexpensive and easy to fabricate. Besides graphene, other carbon-based materials like a carbon nanotube (CNT) may also be considered for integration with metallic plasmonic nanostructures. Even polymers like PMMA, PDMS, SU-8 can be formed as a suspended nanowire system by methods like electrospinning over a trench waveguide to couple with external forces like acoustic wave or vibration that can be optically

detected by the waveguide–nanowire interaction facilitating a compact and an efficient on-chip detection system.

Funding. Defense Threat Reduction Agency (HDTRA1-16-1-0025); National Science Foundation (ECCS-1449397).

Disclosures. The authors declare no conflicts of interest.

REFERENCES

1. C. L. Tan and H. Mohseni, "Emerging technologies for high performance infrared detectors," Nanophotonics **7**, 169–197 (2018).
2. M. Z. Tidrow, W. A. Beck, W. W. Clark, H. K. Pollehn, J. W. Little, N. K. Dhar, R. P. Leavitt, S. W. Kennerly, D. W. Beekman, A. C. Goldberg, and W. R. Dyer, "Device physics and focal plane array applications of QWIP and MCT," Proc. SPIE **3629**, 100–114 (1999).
3. N. Youngblood, C. Chen, S. J. Koester, and M. Li, "Waveguide-integrated black phosphorus photodetector with high responsivity and low dark current," Nat. Photonics **9**, 247–252 (2015).
4. W. C. Tan, L. Huang, R. J. Ng, L. Wang, D. M. N. Hasan, T. J. Duffin, K. S. Kumar, C. A. Nijhuis, C. Lee, and K.-W. Ang, "A black phosphorus carbide infrared phototransistor," Adv. Mater. **30**, 1705039 (2018).
5. X. Yu, P. Yu, D. Wu, B. Singh, Q. Zeng, H. Lin, W. Zhou, J. Lin, K. Suenaga, Z. Liu, and Q. J. Wang, "Atomically thin noble metal dichalcogenide: a broadband mid-infrared semiconductor," Nat. Commun. **9**, 1545 (2018).
6. B. Y. Zhang, T. Liu, B. Meng, X. Li, G. Liang, X. Hu, and Q. J. Wang, "Broadband high photoresponse from pure monolayer graphene photodetector," Nat. Commun. **4**, 1811 (2013).
7. U. Sassi, R. Parret, S. Nanot, M. Bruna, S. Borini, D. De Fazio, Z. Zhao, E. Lidorikis, F. H. L. Koppens, A. C. Ferrari, and A. Colli, "Graphene-based mid-infrared room-temperature pyroelectric bolometers with ultrahigh temperature coefficient of resistance," Nat. Commun. **8**, 14311 (2017).
8. X. Wang, P. Wang, J. Wang, W. Hu, X. Zhou, N. Guo, H. Huang, S. Sun, H. Shen, T. Lin, M. Tang, L. Liao, A. Jiang, J. Sun, X. Meng, X. Chen, W. Lu, and J. Chu, "Ultrasensitive and broadband MoS_2 photodetector driven by ferroelectrics," Adv. Mater. **27**, 6575–6581 (2015).
9. M. Furchi, A. Urich, A. Pospischil, G. Lilley, K. Unterrainer, H. Detz, P. Klang, A. M. Andrews, W. Schrenk, G. Strasser, and T. Mueller, "Microcavity-integrated graphene photodetector," Nano Lett. **12**, 2773–2777 (2012).
10. E. Steveler, M. Verdun, B. Portier, P. Chevalier, C. Dupuis, N. Bardou, J.-B. Rodriguez, R. Haïdar, F. Pardo, and J.-L. Pelouard, "Optical index measurement of InAs/GaSb type-II superlattice for mid-infrared photodetection at cryogenic temperatures," Appl. Phys. Lett. **105**, 141103 (2014).
11. R. S. Attaluri, J. Shao, K. T. Posani, S. J. Lee, J. S. Brown, A. Stintz, and S. Krishna, "Resonant cavity enhanced InAs/In0.15ga0.85as dots-in-a-well quantum dot infrared photodetector," J. Vacuum Sci. Technol. B **25**, 1186–1190 (2007).
12. C.-C. Wang and S.-D. Lin, "Resonant cavity-enhanced quantum-dot infrared photodetectors with sub-wavelength grating mirror," J. Appl. Phys. **113**, 213108 (2013).
13. W. Wang, A. Klots, Y. Yang, W. Li, I. I. Kravchenko, D. P. Briggs, K. I. Bolotin, and J. Valentine, "Enhanced absorption in two-dimensional materials via Fano-resonant photonic crystals," Appl. Phys. Lett. **106**, 181104 (2015).
14. S. Cakmakyapan, P. K. Lu, A. Navabi, and M. Jarrahi, "Gold-patched graphene nano-stripes for high-responsivity and ultrafast photodetection from the visible to infrared regime," Light Sci. Appl. **7**, 20 (2018).
15. W. Li and J. Valentine, "Metamaterial perfect absorber based hot electron photodetection," Nano Lett. **14**, 3510–3514 (2014).
16. Z. Qian, Y. Hui, F. Liu, S. Kang, S. Kar, and M. Rinaldi, "Graphene–aluminum nitride NEMS resonant infrared detector," Microsyst. Nanoeng. **2**, 1–7 (2016).
17. A. D. Pris, Y. Utturkar, C. Surman, W. G. Morris, A. Vert, S. Zalyubovskiy, T. Deng, H. T. Ghiradella, and R. A. Potyrailo, "Towards high-speed imaging of infrared photons with bio-inspired nanoarchitectures," Nat. Photonics **6**, 195 (2012).
18. A. Rogalski, "Recent progress in infrared detector technologies," Infrared Phys. Technol. **54**, 136–154 (2011).
19. J. L. Corbeil, N. V. Lavrik, S. Rajic, and P. G. Datskos, "Self-leveling" uncooled microcantilever thermal detector," Appl. Phys. Lett. **81**, 1306–1308 (2002).
20. P. Eriksson, J. Y. Andersson, and G. Stemme, "Thermal characterization of surface-micromachined silicon nitride membranes for thermal infrared detectors," J. Microelectromech. Syst. **6**, 55–61 (1997).
21. J. B. Herzog, M. W. Knight, and D. Natelson, "Thermoplasmonics: quantifying plasmonic heating in single nanowires," Nano Lett. **14**, 499–503 (2014).
22. Z. Qian, S. Kang, V. Rajaram, C. Cassella, N. E. McGruer, and M. Rinaldi, "Zero-power infrared digitizers based on plasmonically enhanced micromechanical photoswitches," Nat. Nanotechnol. **12**, 969–973 (2017).
23. W. Dai, Q. Yang, F. Gu, and L. Tong, "ZnO subwavelength wires for fast-response mid-infrared detection," Opt. Express **17**, 21808–21812 (2009).
24. F. Zhang, Q. Shen, X. Shi, S. Li, W. Wang, Z. Luo, G. He, P. Zhang, P. Tao, C. Song, W. Zhang, D. Zhang, T. Deng, and W. Shang, "Infrared detection based on localized modification of morpho butterfly wings," Adv. Mater. **27**, 1077–1082 (2015).
25. F. Yi, H. Zhu, J. C. Reed, and E. Cubukcu, "Plasmonically enhanced thermomechanical detection of infrared radiation," Nano Lett. **13**, 1638–1643 (2013).
26. J. Valente, J.-Y. Ou, E. Plum, I. J. Youngs, and N. I. Zheludev, "A magneto-electro-optical effect in a plasmonic nanowire material," Nat. Commun. **6**, 7021 (2015).
27. K. Zhou, X. Wang, X. Sun, Q. Peng, and Y. Li, "Enhanced catalytic activity of ceria nanorods from well-defined reactive crystal planes," J. Catal. **229**, 206–212 (2005).
28. J.-Y. Ou, E. Plum, J. Zhang, and N. I. Zheludev, "Giant nonlinearity of an optically reconfigurable plasmonic metamaterial," Adv. Mater. **28**, 729–733 (2016).
29. A. Persano, B. Nabet, A. Taurino, P. Prete, N. Lovergine, and A. Cola, "Polarization anisotropy of individual core/shell GaAs/AlGaAs nanowires by photocurrent spectroscopy," Appl. Phys. Lett. **98**, 153106 (2011).
30. H. Pettersson, J. Trägårdh, A. I. Persson, L. Landin, D. Hessman, and L. Samuelson, "Infrared photodetectors in heterostructure nanowires," Nano Lett. **6**, 229–232 (2006).
31. J. Wang, M. S. Gudiksen, X. Duan, Y. Cui, and C. M. Lieber, "Highly polarized photoluminescence and photodetection from single indium phosphide nanowires," Science **293**, 1455–1457 (2001).
32. S. Ogawa and M. Kimata, "Metal-insulator-metal-based plasmonic metamaterial absorbers at visible and infrared wavelengths: a review," Materials **11**, 458 (2018).
33. G. Tagliabue, H. Eghlidi, and D. Poulikakos, "Facile multifunctional plasmonic sunlight harvesting with tapered triangle nanopatterning of thin films," Nanoscale **5**, 9957–9962 (2013).
34. H. Zhu, F. Yi, and E. Cubukcu, "Plasmonic metamaterial absorber for broadband manipulation of mechanical resonances," Nat. Photonics **10**, 709–714 (2016).
35. J. J. Talghader, A. S. Gawarikar, and R. P. Shea, "Spectral selectivity in infrared thermal detection," Light: Sci. Appl. **1**, e24 (2012).
36. J. W. Stewart, J. H. Vella, W. Li, S. Fan, and M. H. Mikkelsen, "Ultrafast pyroelectric photodetection with on-chip spectral filters," Nat. Mater. **19**, 158–162 (2019).
37. N. Liu, M. Mesch, T. Weiss, M. Hentschel, and H. Giessen, "Infrared perfect absorber and its application as plasmonic sensor," Nano Lett. **10**, 2342–2348 (2010).
38. Q. Zhao, M. W. Khan, S. Farzinazar, J. Lee, and O. Boyraz, "Plasmo-thermomechanical radiation detector with on-chip optical readout," Opt. Express **26**, 29638 (2018).
39. M. W. Khan, P. Sadri-Moshkenani, M. S. Islam, and O. Boyraz, "Graphene-coated suspended metallic nanostructures for fast and sensitive optomechanical infrared detection," in *Conference on*

Lasers and Electro-Optics (CLEO): Science and Innovations, San Jose, CA, USA (Optical Society of America, 2019), paper JTu2A-51.
40. A. A. Balandin, S. Ghosh, W. Bao, I. Calizo, D. Teweldebrhan, F. Miao, and C. N. Lau, "Superior thermal conductivity of single-layer graphene," Nano Lett. **8**, 902–907 (2008).
41. E. Pop, V. Varshney, and A. K. Roy, "Thermal properties of graphene: fundamentals and applications," MRS Bull. **37** (12), 1273–1281 (2012).
42. L. A. Falkovsky, "Optical properties of graphene," J. Phys. **129**, 012004 (2008).
43. I. W. Frank, D. M. Tanenbaum, A. M. van der Zande, and P. L. McEuen, "Mechanical properties of suspended graphene sheets," J. Vacuum Sci. Technol. B **25**, 2558–2561 (2007).
44. D. G. Papageorgiou, I. A. Kinloch, and R. J. Young, "Mechanical properties of graphene and graphene-based nanocomposites," Progr. Mater. Sci. **90**, 75–127 (2017).
45. Y. Liu, R. Cheng, L. Liao, H. Zhou, J. Bai, G. Liu, L. Liu, Y. Huang, and X. Duan, "Plasmon resonance enhanced multicolour photodetection by graphene," Nat. Commun. **2**, 579 (2011).
46. T. J. Echtermeyer, L. Britnell, P. K. Jasnos, A. Lombardo, R. V. Gorbachev, A. N. Grigorenko, A. K. Geim, A. C. Ferrari, and K. S. Novoselov, "Strong plasmonic enhancement of photovoltage in graphene," Nat. Commun. **2**, 458 (2011).
47. M. Hashemi, M. H. Farzad, N. A. Mortensen, and S. Xiao, "Enhanced absorption of graphene in the visible region by use of plasmonic nanostructures," J. Opt. **15**, 055003 (2013).
48. M. Liu, X. Yin, E. Ulin-Avila, B. Geng, T. Zentgraf, L. Ju, F. Wang, and X. Zhang, "A graphene-based broadband optical modulator," Nature **474**, 64–67 (2011).
49. L. A. Falkovsky and S. S. Pershoguba, "Optical far-infrared properties of a graphene monolayer and multilayer," Phys. Rev. B **76**, 153410 (2007).
50. J. Chen, P. Albella, Z. Pirzadeh, P. Alonso-Gonzźlez, F. Huth, S. Bonetti, V. Bonanni, J. Åkerman, J. Nogués, P. Vavassori, A. Dmitriev, J. Aizpurua, and R. Hillenbrand, "Plasmonic nickel nanoantennas," Small **7**, 2341–2347 (2011).
51. L. Cui, S. Shi, Z. Li, G. Wei, and X. Du, "Manipulating thermal conductance of supported graphene via surface hydroxylation of substrates," J. Phys. Chem. C **122**, 27689–27695 (2018).
52. Z. Gao, Y. Zhang, Y. Fu, M. Yuen, and J. Liu, "Graphene heat spreader for thermal management of hot spots," in *IEEE 63rd Electronic Components and Technology Conference*, Las Vegas, NV, USA (2013), pp. 2075–2078.
53. G. Chen, C. L. Tien, X. Wu, and J. S. Smith, "Thermal diffusivity measurement of GaAs/AlGaAs thin-film structures," J. Heat Transfer **116**, 325–331 (1994).
54. J. G. Hust and P. J. Giarratano, "Thermal conductivity and electrical resistivity standard reference materials: tungsten SRM's 730 and 799, from 4 to 3000K. Final report," NBS Special Publication 260-52 (National Bureau of Standards, 1994).
55. Y. Shiping and J. Peixue, "Thermal conductivity of nanoscale thin nickel films," Prog. Nat. Sci. **15**, 922–929 (2005).